Techno-computing Journal 2(2) 59-78 (2026)
https://doi.org/10.71170/tecoj.2026.2.2.59-78

Research Paper

Numerical Simulation of a Lead-Free $FASnI_3$ Perovskite Solar Cell with CeO_2 Electron Transport Layer Achieving 22.29% Power Conversion Efficiency Using SCAPS-1D

Mannir Abubakar Ahmad[1]*, Zakiyyu Ibrahim Takai[1], Hamza Mustapha Umar[1], Maimuna Aliyu Abubakar[1]

[1]*Faculty of Science, Department of Physics, Northwest University, Kano, Kano State, Nigeria*

**Corresponding Author Email:* maahmad@nwu.edu.ng

Abstract

This paper presents a physics-based simulation of a lead-free $FASnI_3$ Perovskite Solar Cell (PSC) using Solar Cell Capacitance Simulator One-Dimension (SCAPS-1D). Six device parameters were systematically investigated: the absorber band gap, the layer thickness, bulk defect density (N_t), the operating temperature, the series resistance (R_s) and the shunt resistance (R_{sh}). The device Short-circuit Current Density (J_{sc}) was determined to be 28.73 mA/cm², Open-circuit Voltage (V_{oc}) = 0.9862 V, Fill Factor (FF) = 78.68%, and Power Conversion Efficiency (PCE) = 22.29%. A conduction band cliff of −0.60 eV at the CeO_2/$FASnI_3$ interface and a valence band cliff of −0.19 eV at the $FASnI_3$/NiO interface were found, which promote interfacial recombination and limit the FF; the effect of the interface band offsets and interface defect density on the device performance was quantified. It was observed that bulk defect density is the most critical parameter limiting the device performance, with PCE = 7.72% at $N_t = 10^{20}$ cm^{-3}; it is evident that N_t needs to be reduced below 10^{16} cm^{-3} for PCE > 20%. V_{oc} varied by only 5.1 mV (0.9828–0.9879 V) and the PCE changed over 280–310 K, whereas the PCE was degraded significantly at R_{sh} < 1000 Ω·cm² and R_s > 2 Ω·cm². The absorption edge was confirmed by quantum efficiency, which is around 855 nm. The targets for improvement are: $FASnI_3$/NiO interface passivation, reduction of N_t, and electron transport layer (ETL) work-function engineering (χ = 4.2–4.3 eV).

Keywords: Shockley–Read–Hall recombination; Bulk defect density; Carrier diffusion length; CeO_2 electron transport layer; NiO hole transport layer; Quantum efficiency.

1. Introduction

Photovoltaic (PV) technology has recently become the most important renewable energy research and policy investment in the world today; the transition to decarbonised energy systems has gained momentum [1]. Perovskite solar cells (PSCs) belong to the group of upcoming PV technologies and have shown an unprecedented efficiency improvement from a certified PCE of 3.8% in 2009 to 26% in tandem devices in 2024 [2,3,28]. It is based on the intrinsic properties of the ABX_3 crystal structure, which are unique to these materials: a tunable direct bandgap (1.2-3.0 eV), high absorption coefficient (>10^5 cm^{-1}), long ambipolar carrier diffusion length and low-temperature solution-based fabrication [4,5]. The most common and highly efficient PSCs are lead halides. However, due to lead's toxic nature, the devices face a significant limitation at every stage in their life cycle, delaying commercialisation [2]. This has led to extensive research on lead-free materials, particularly tin-based, such as formamidinium tin iodide ($FASnI_3$), which is the most promising [6]. $FASnI_3$ is a direct bandgap semiconductor with an optimum of ~1.41 eV, near the Shockley–Queisser single-junction optimum; it has a high ambipolar carrier mobility of ~20 cm^2 V^{-1} s^{-1}, and much lower toxicity [7,8]. The FA^+ cation is more effective in stabilising the 3D perovskite structure than MA^+ [9], which helps to reduce the thermally induced phase transitions.

(Received 25 June 2026; revised 21 August 2026; accepted 31 August 2026; first published online10 October 2026);
©Techno-computing Journal 2026. Journal homepage https://technocomputing.org/index.php/tecoj

Tin-based PSCs, especially $FASnI_3$ devices, suffer from low power conversion efficiency caused by several factors, including non-radiative Shockley–Read–Hall (SRH) recombination centre states, which significantly shorten the carrier lifetimes and decrease the Voc [10,11]. The cerium oxide (CeO_2) layer is used as the electron transport layer (ETL) in the device architecture, which has a wide bandgap (= 3.5 eV), is very stable and can be processed without any annealing [12]. Nickel oxide (NiO) is used as the hole transport layer (HTL), which has a deep valence band and has higher inorganic stability than spiro-OMeTAD (2,2′,7,7′-tetrakis(N,N-di-p-methoxyphenylamine)-9,9′-spirobifluorene) [13]. The back contact is gold (Au), which is chosen due to its high electrical conductivity, low contact resistance and good chemical stability. Numerical simulation of PSC devices using Solar Cell Capacitance Simulator in One Dimension (SCAPS-1D) is an indispensable tool for evaluating solar-cell devices [15,37]. While many studies have been conducted on lead-free solar cells, most have considered the individual effects of device parameters such as electron transport layers or optimising parameters one by one [14,20,30,35], and a detailed investigation of the combined effect of absorber bandgap, absorber thickness, bulk defect density, operating temperature, series resistance and shunt resistance in a CeO_2/NiO-based architecture is still limited. The fluorine-doped tin oxide (FTO)/CeO_2/$FASnI_3$/NiO/Au architecture, to the best of the authors' knowledge, has not been previously characterised. The aim of the present study is then to systematically investigate these six device parameters using the J–V characteristics, recombination current density analysis, energy band alignment and quantum efficiency characterisation and to identify the dominant performance-limiting mechanisms, and to convert them into quantitative design targets for the fabrication of high-performance lead-free $FASnI_3$ solar cells.

2. Device Structure and Simulation Methodology

2.1 Device Architecture

The device structure is shown in Fig. 1: FTO/CeO_2/$FASnI_3$/NiO/Au, a planar n-i-p heterojunction: FTO (front contact, φ = 4.4 eV) → CeO_2 (ETL) → $FASnI_3$ (absorber) → NiO (HTL) → Au (rear contact, φ = 5.1 eV) (Figure 1).

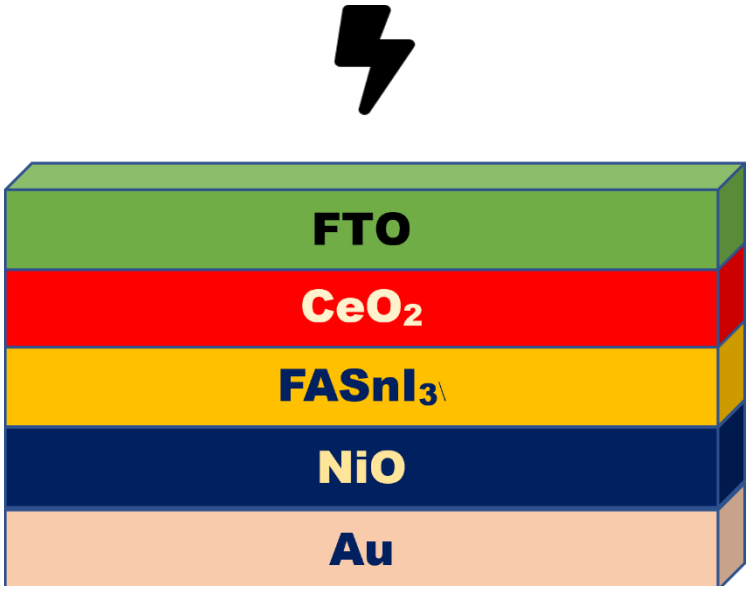


Figure 1: Schematic device structure of the FTO/CeO_2/$FASnI_3$/NiO/Au n-i-p planar perovskite solar cell.

2.2. SCAPS-1D Simulation Framework

The simulations were performed using SCAPS-1D version 3.3.10 [15,21,43], solving the Poisson equation (1) and the hole and electron continuity equations (2 and 3):

$$\frac{d}{dx}\left[\varepsilon(\chi)\frac{d\psi}{dx}\right] = q[p(x) - n(x) + N_D(x) - N_A(x) + P_t(x) - n_t(x)] \quad (1)$$

$$\left(\frac{1}{q}\right)\left(\frac{\partial Jp}{\partial x}\right) + Rp(x) - G(x) = 0 \quad (2)$$

$$-\left(\frac{1}{q}\right)\left(\frac{\partial Jn}{\partial x}\right) + \boldsymbol{Rn(x)} - \boldsymbol{G(x)} = \mathbf{0} \quad (3)$$

where ε(x) is the spatially dependent permittivity, ψ is the electrostatic potential, q is the elementary charge, P and n are the free-hole and free-electron concentrations, respectively, and ND+ and NA- are ionised donor and acceptor concentrations. The quantities Pt and nt are the trapped-hole and trapped-electron concentrations, respectively. Jp and Jn are the hole and electron current densities, R is the net recombination rate under the adopted sign convention, and G(x) is the position-dependent photogeneration rate [16]. The governing equations are solved self-consistently to obtain the electrostatic potential, carrier distributions and current-voltage characteristics. Recombination mechanisms included are radiative band-to-band, Auger, and SRH trap-assisted recombination. All simulations were conducted under AM 1.5G illumination at 100 mW/cm² and 300 K. The modified diode equation incorporating parasitic resistances is:

$$\boldsymbol{J = J_P h - J_o \left[exp\left(\frac{q(V+JR_S)}{nKT}\right) - 1\right] - \left(\frac{V+JR_S}{R_{SH}}\right)} \quad (4)$$

Where J is the current density, V is the terminal voltage, Jp*h* is the photogenerated current density, Jo is the dark saturation current, n is the diode ideality factor, Rs is area normalized series resistance, Rsh is area-normalized shunt resistance, k is Boltzmann's constant, and T is the absolute temperature expressed in Kelvin (K) [22]. This equation assumes current density is positive in the photocurrent-generating direction and that the resistances are expressed in ohm-square centimetres (Ω·cm^2). The Fill Factor (FF) is calculated as the ratio of the maximum electrical power to the product of the open-circuit voltage and short-circuit current:

$$\boldsymbol{FF = \frac{(V_{MP} \times J_{MP})}{(V_{OC} \times J_{SC})}} \quad (5)$$

Where VMP and JMP are the voltage and current at the maximum power point, respectively, and VOC and JSC are the open-circuit voltage and short-circuit current density.

The Power Conversion Efficiency (PCE) is calculated as

$$\boldsymbol{PCE}\ (\%) = \left(\frac{V_{OC} \times J_{SC} \times FF}{P_{in}}\right) \times \mathbf{100}\% \quad (6)$$

Where Pin is the incident optical power density. FF is expressed as a dimensionless fraction in the PCE equation. Under standard AM 1.5G illumination. Pin = 100 mWcm-2

2.3 Material Parameters and Parametric Study Summary

The material parameters used are presented in Table 1 below. Neutral discrete mid-gap traps at 0.6 eV above the valence band edge with capture cross sections of 1.0×10^{-15} cm² and baseline interface trap density of 1.0×10^{10} cm^{-2} are considered to be interface defect states at both heterojunctions [16]. For each parametric study, only the variable being changed is changed; other variables are kept at their Table 1 base values.

Table 1. Baseline material parameters for each layer of the FTO/CeO2/FASnI3/NiO/Au device [16,23,24]

Parameter	FTO	CeO_2 (ETL)	$FASnI_3$ (Absorber)	NiO (HTL)
Thickness (nm)	400	450	500–1000 (varied)	100
Bandgap Eg (eV)	3.50	3.50	1.45 (varied)	3.80
Electron affinity χ (eV)	4.30	4.60	4.00	1.46
Relative permittivity ε_r	9.0	9.0	8.2	10.7
CB eff. density Nc (cm^{-3})	2.2×10^{18}	1.0×10^{20}	1.0×10^{18}	2.8×10^{19}

VB eff. density NV (cm^{-3})	1.8×10^{19}	2.0×10^{21}	1.0×10^{18}	1.0×10^{19}
Electron mobility (cm^2/Vs)	20	100	22	1.2
Hole mobility (cm^2/Vs)	10	25	22	2.8
Donor density ND (cm^{-3})	1.0×10^{18}	1.0×10^{21}	0	0
Acceptor density NA (cm^{-3})	0	0	7.0×10^{16}	1.0×10^{18}
Bulk defect density Nt (cm^{-3})	—	1.0×10^{15}	1.0×10^{15} (varied)	1.0×10^{15}
Thermal velocity (cm/s)	1.0×10^{7}	1.0×10^{7}	1.0×10^{7}	1.0×10^{7}

3. Results and Discussions

3.1 Device Structure and Equilibrium Band Alignment

The schematic layer sequence of the device is presented in Figure 2. The band offsets at both heterojunctions were calculated from the material parameters in Table 1 because they influence charge selectivity, interfacial recombination and fill factor. At the $FASnI_3$/NiO heterojunction, the ionisation potential of $FASnI_3$ ($\chi + Eg = 4.0 + 1.45 = 5.45$ eV) exceeds that of NiO ($\chi + Eg = 1.46 + 3.80 = 5.26$ eV), producing a valence band offset of $\Delta EV = -0.19$ eV (cliff-type) at the absorber/HTL interface. In a cliff configuration, the HTL valence band maximum is higher than that of the absorber, allowing the transfer of holes without a classical injection barrier, and at the same time eliminating the local field discontinuity that would otherwise drive minority electrons away from this interface, allowing a recombination path for the photogenerated electrons arriving at the absorber/HTL interface before extraction [27]. The FF of 78.68% is below the interface-recombination-free value of about 86–88% estimated using the Green analytical expression [38]. The calculated band offsets provide a possible explanation for part of this difference; however, the individual contribution of interface recombination was not isolated or quantified in this study. The interface defect density was held at its baseline value rather than varied independently. Interface passivation may therefore be a potential strategy for reducing recombination losses in a future experimental device; this possibility was not tested in the present simulation. The carrier lifetime at the baseline $Nt = 10^{15}$ cm^{-3} is estimated from $\tau = 1/(Nt\sigma v_{th}) = 1/(10^{15} \times 10^{-15} \times 10^{7}) = 100$ ns, yielding an ambipolar diffusion length $L = \sqrt{(kT/q \times \mu \times \tau)} = \sqrt{(0.026 \times 22 \times 10^{-7})} = 2.4$ μm (2392 nm), consistent with the long carrier diffusion lengths reported for halide perovskite absorbers [31]. Most of the photogenerated carriers can reach the transport layers at the baseline $Nt = 10^{15}$ cm-3, because the estimated diffusion length L is larger than the baseline absorber thickness $t_{abs} = 1000$ nm (Section 3.3, Figs. 6–7). The device is expected to enter the diffusion-limited regime as Nt increases; from the above, it can be seen that the crossover is at $Nt = 5.7 \times 10^{15}$ cm^{-3}, where Jsc is expected to be reduced by incomplete carrier collection. All the parametric studies of Nt in this work are based on this diffusion-length constraint.

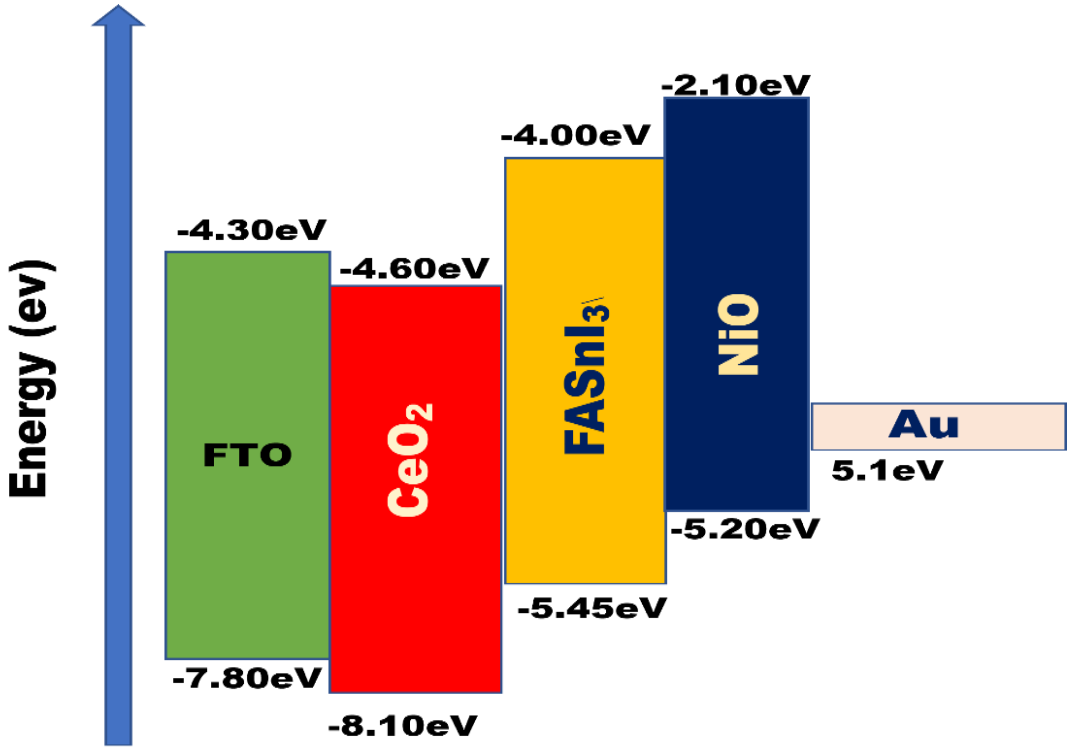


Figure 2: Schematic layer sequence of the FTO/CeO2/FASnI3/NiO/Au device.

3.2. Effect of FASnI3 Absorber Bandgap

The percentage of the solar spectrum absorbed and the maximum achievable open-circuit voltage (Voc) of a PV device are determined by the bandgap (Eg) of the absorber layer, which underpins the fundamental efficiency trade-off inherent in PV device physics [2]. A smaller bandgap means that a higher percentage of AM 1.5G photons are absorbed, raising Jsc, but reducing the thermodynamic driving force to separate carriers, reducing Voc. The Shockley–Queisser detailed balance calculation suggests that the optimal single-junction bandgap is 1.1–1.4 eV for AM 1.5G illumination, and FASnI3 is determined to be near the optimal bandgap (1.41–1.45 eV) [7]. The other parameters were kept at the baseline values presented in Table 1, and the thickness of the absorber was fixed at 1000 nm, while the FASnI3 bandgap was varied by 0.01 eV. The results are shown in Fig. 3 and Table 2).

Table 2. Simulated photovoltaic parameters as a function of FASnI3 absorber bandgap Eg at 300 K.

E_g (eV)	V_{oc} (V)	J_{sc} (mA/cm²)	FF (%)	PCE (%)
1.45	0.9862	28.73	78.68	22.29
1.44	0.9742	29.01	74.43	21.03
1.43	0.9651	29.52	74.15	21.13
1.42	0.9549	29.90	73.97	21.04
1.41	0.9443	30.28	72.71	20.79

Voc decreases monotonically as Eg narrows, declining from 0.9862 V at 1.45 eV to a predicted 0.9443 V at 1.41 eV — a total reduction of 41.9 mV corresponding to a linear rate of 10.5 mV per 0.01 eV (R^2 = 0.997). This almost linear dependence of Voc on the bandgap is a direct consequence of the dependence of both the upper bound and the quasi-Fermi level splitting under illumination on the bandgap: Voc = Eg/q − (nkT/q) ln (NcNv/Jph): as Eg decreases, both the upper bound and the quasi-Fermi level splitting under illumination decrease proportionally [33]. This is a narrow range over which the bandgap term dominates the recombination-driven changes in J0.Jsc increases monotonically from 28.73 mA/cm² at 1.45 eV to a predicted 30.28 mA/cm² at 1.41 eV, a gain of 1.55 mA/cm² (R^2 = 0.985).

This is due to the extension of the optical absorption edge towards longer wavelengths: λedge = 1240/Eg ranges from 855 nm at 1.45 eV to 879 nm at 1.41 eV, allowing photons to be harvested in an additional 24 nm near-infrared window. In this narrow near-IR range, the AM 1.5G spectrum is approximately linear, and the Beer–Lambert optical generation model in SCAPS-1D shows this extension.

The fill factor shows a significant sharp drop from 78.68% at 1.45 eV to 74.43% at 1.44 eV, followed by a nearly flat plateau at around 74.15% and 73.97% at 1.43 eV and 1.42 eV, respectively, with a discontinuity of 4.25 percentage points for a 0.01 eV change in the bandgap. This two-regime behavior is of physical interest. The initial sharp drop in FF at 1.44 eV is attributed to the increased contribution of the trap-assisted SRH recombination to the ideality factor as the bandgap narrows: A fixed trap energy Eτ and fixed Ntσvth cause the ratio of the thermal generation rate to the optical generation rate to rise near the trap energy as Eg decreases, thereby increasing the SRH contribution to current flow near the maximum power point and thus affecting the J–V curve [36]. The following plateau at 1.43–1.42 eV indicates a partial balance between the rise in photocurrent density and the increase in the ideality factor due to recombination, resulting in an almost equal balance of FF.

PCE shows a non-monotonic trend: it reaches 22.29% at 1.45 eV, and then decreases to 21.03% at 1.44 eV due to the sharp FF reduction, after which it increases slightly to 21.13% at 1.43 eV, stabilises around 21.04% at 1.42 eV, and is expected to drop again to 20.79% at 1.41 eV. This behaviour, showing a baseline bandgap of 1.45 eV, results in maximum PCE in the configuration of FTO/CeO_2/$FASnI_3$/NiO/Au when NiO is used as a HTL. The photocurrent gain is not enough to compensate for the FF penalty due to bandgap narrowing caused by the interaction between the narrower Eg and the fixed $FASnI_3$/NiO valence band cliff found in Section 3.1, which is not considered in the Shockley–Queisser analysis [2].

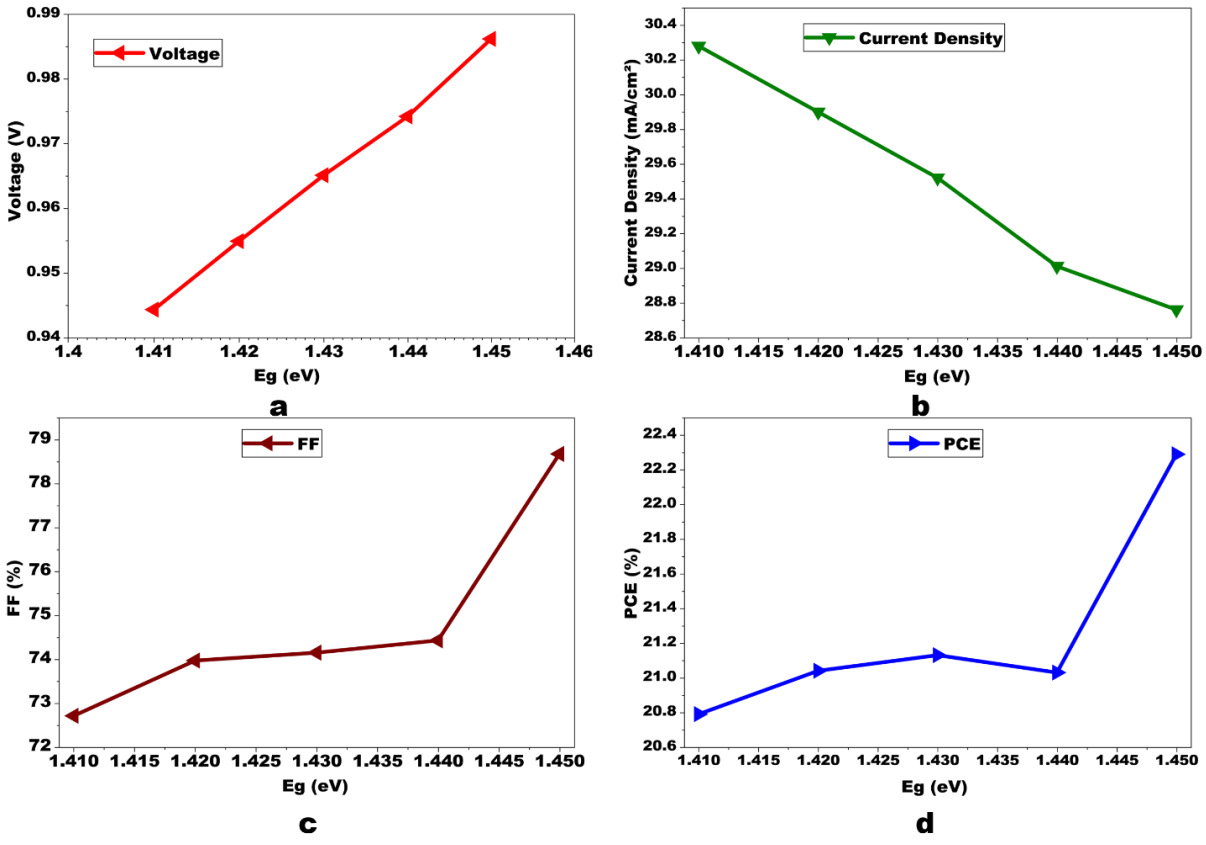


Figure 3: *Simulated photovoltaic parameters (a) V_{oc}, (b) J_{sc}, (c) FF, and (d) PCE as functions of $FASnI_3$ absorber bandgap from 1.45 eV to 1.41 eV.*

The J–V characteristics of each bandgap value are shown in Fig. 4. There are several features of the family of curves which are physically significant and are complementary to and supported by the parametric features given in Table 2. The five curves are nearly parallel in the flat plateau region of photocurrent (0 to ~0.7 V), with each curve being displaced from the next wider bandgap curve by the current magnitude difference. The variation of the bandgap in this range is seen to affect the photogenerated carrier density, due to the extension of the Beer–Lambert absorption edge from 855

nm to 879 nm, rather than the change in the low-bias carrier transport and recombination kinetics—the photocurrent plateau at low forward bias is determined solely by the photogeneration process, the progressive upward shift of photocurrent from 28.73 mA/cm² at 1.45 eV to 30.28 mA/cm² at 1.41 eV is therefore a direct measure of the additional photon flux harvested as the absorption edge extends from 855 nm to 879 nm [32]. The Voc intercepts gradually shift to the left with a linear rate of 10.5 mV/0.01 eV (Table 2) as the bandgap decreases, and are clearly seen in the five different zero-crossing points of the J–V curves in Fig. 4. The shape of the knee in the maximum power point region (MPPR) (around 0.85V to Voc for each curve) is the most significant feature of the J–V curves for diagnosis. The knee is the sharpest and the most rectangular in the family with the highest FF (78.68%) and the closest ideality factor to unity (1.45 eV). The change in the knee shape from 1.45 to 1.44 eV corresponds to a more rounded knee (most prominent change in the knee shape between two consecutive transitions in the family that has a sharp FF discontinuity at 1.44 eV, as listed in Table 2). The J–V shows a signature of a higher ideality factor, as a higher n makes the knee more gradual, and the area under the curve and the power axis will decrease closer to Voc [39]. The curves of 1.43, 1.42 and 1.41 eV exhibit increasingly but less sharply rounded knees, consistent with the almost flat FF plateau of 73.97–74.15% observed in these band gaps in Table 2. As the bandgap decreases, the maximum power point of each curve progressively moves downward and leftward, indicating the opposing trends of increasing Jmpp and decreasing Vmpp, and the product Jmpp × Vmpp peaks at 1.45 eV and then decreases with further reductions in bandgap, establishing the 1.45 eV baseline as the highest-PCE configuration in this architecture.

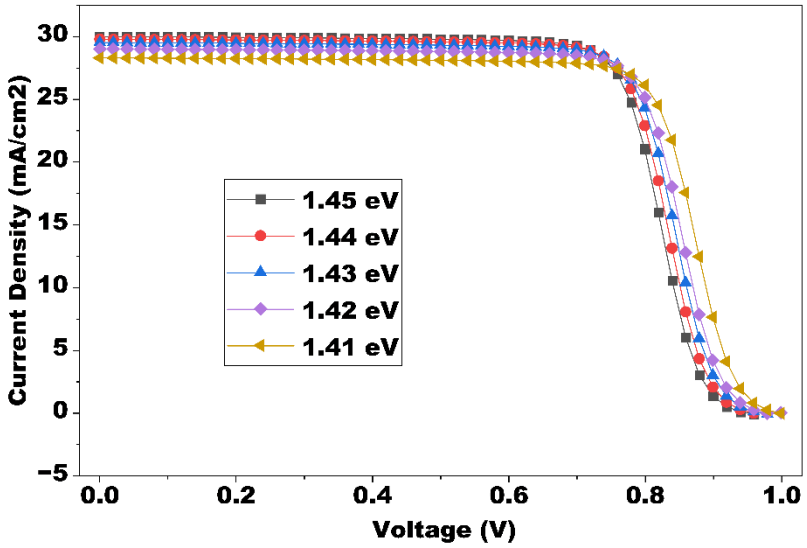


Figure 4: Simulated J–V characteristics of the FTO/CeO2/FASnI3/NiO/Au device for FASnI3 bandgap values from 1.45 eV to 1.41 eV.

The total recombination current density as a function of applied voltage for each bandgap is shown in Fig. 5. The recombination curves provide a direct physical interpretation of the trends in J–V (shown in Fig. 4) and the trends in the parameters (shown in Table 2). All 5 curves are near zero at forward bias (V < 0.6 V), which indicates that the device is in the photovoltaic regime throughout this voltage range, no matter what bandgap value is used: the photogeneration rate is higher than the recombination rate at all 5 bandgap values at voltages well below Voc, leading to the plateaus in photocurrent seen in Fig. 4 [36]. One of the most interesting and physically significant features of Fig. 5 is the systematic curvature of the recombination onset voltage on the right-hand side, with decreasing bandgap. The onset voltage shifts from ~ 0.90-0.92 V at 1.45 eV to ~0.82-0.84 V at 1.41 eV, which is directly related to the Voc reduction in Table 2. The causal relationship is the most basic property of Voc, which is determined by the condition that Jph = Jrec at the terminals. As the band gap decreases, the recombination current becomes more and more comparable to the photocurrent at lower forward voltage because of the increase in the rate of thermal generation at the trap level (SRH mechanism) ∝ ni(T) exp ((Eg – 2Et)/2kT) in the depletion approximation, resulting in a progressive decrease in Voc [36]. As predicted from physical considerations, all 5 curves tend to the same recombination current density at the Voc intercepts, where the recombination current should be equal to the photocurrent, due to current continuity. The small differences in Jrec at the open-circuit condition are due to the small

differences in Jph between the five bandgap values. Most importantly, at a fixed voltage below Voc (e.g., 0.85 V), the narrower bandgap curves show higher recombination current density than the wider bandgap curves, indicating that the higher SRH contribution at the narrower bandgaps is not only present at Voc but is also present in the maximum power point region. This higher recombination in the MPP region is how the increase in ideality factor at narrower bandgaps manifests itself as the rounded J–V knee and lower FF seen in Fig. 4. The same 1.44 eV curve also shows a slightly higher onset slope in the recombination transition region (between 0.88 V and 0.97 V) which was also observed in the adjacent 1.43 eV and 1.45 eV curves, and which provides further evidence of the sharp drop in FF at 0.88 V – 0.97 V identified in Table 2, as being the result of a qualitative change in the recombination mechanism, specifically an increased SRH ideality factor contribution at the 1.44 eV threshold.

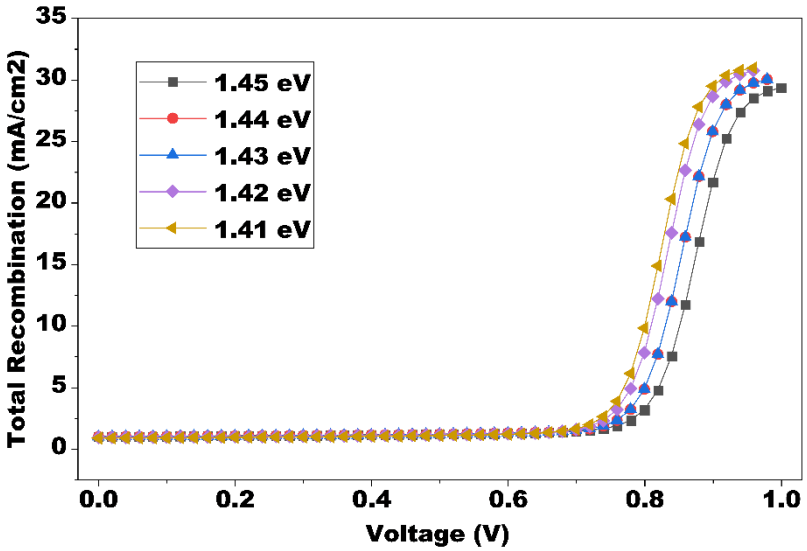


Figure 5: Simulated total recombination current density as a function of applied voltage for $FASnI_3$ bandgap values from 1.45 eV to 1.41 eV.

3.3 Effect of $FASnI_3$ Absorber Layer Thickness

The absorber layer thickness determines three competing performance factors: the optical path length available for photon absorption (Beer–Lambert law: $I(x) = I_0 \exp(-\alpha x)$); the average carrier transport distance to the extraction contacts; and the volume available for bulk SRH recombination. The $FASnI_3$ absorber thickness was evaluated from 500 nm to 1000 nm in 100 nm steps with all other parameters at Table 1 baseline values. Results are in Table 3 and Fig. 6.

Table 3. Simulated photovoltaic parameters as a function of $FASnI_3$ absorber thickness at 300 K.

Thickness (nm)	V_{oc} (V)	J_{sc} (mA/cm²)	FF (%)	PCE (%)
500	0.9852	26.80	79.38	20.96
600	0.9858	27.57	79.20	21.52
700	0.9861	28.06	79.05	21.87
800	0.9862	28.38	78.91	22.09
900	0.9862	28.59	78.79	22.22

1000	0.9862	28.73	78.68	22.29

The Jsc increases monotonically from 26.80 mA/cm² at 500 nm to 28.73 mA/cm² at 1000 nm, a gain of 1.93 mA/cm². As expected from Beer–Lambert saturation, as the absorption efficiency increases towards unity for near-gap photons, the rate of improvement decreases with thickness (0.77, 0.49, 0.32, 0.21, 0.14 mA/cm² per 100 nm). Voc plateaus at 0.9862 V above 800 nm. The plateau is explained by the fact that when the absorber approaches complete photon harvesting, Voc = (nkT/q) ln (Jph/J0 + 1), the saturation of Jph, which causes the saturation of Voc, is balanced by the marginal increase of J0 with thickness. The fill factor reduces from 79.38% to 78.68% (a decrease of 0.70 percentage points over the entire thickness range). This small change confirms that the dominant FF limitation in this device is the $FASnI_3$/NiO interface cliff as established in Section 3.1, which does not depend on the absorber thickness but rather on carrier transport resistance through the bulk [34]. The corresponding simulated J–V characteristics for absorber thicknesses from 600 nm to 1000 nm are shown in Fig. 7.

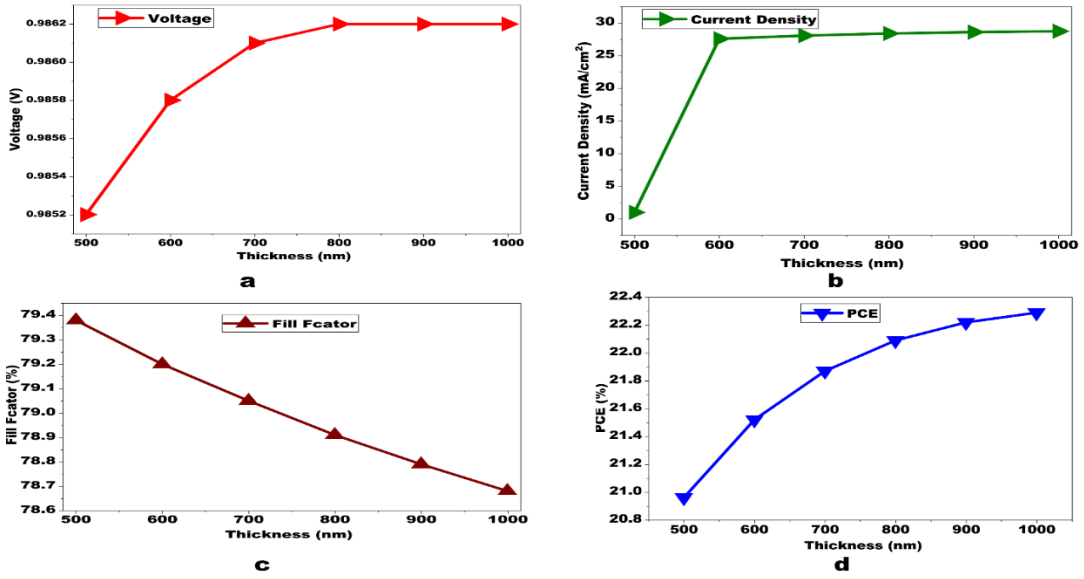


Fig. 6. *Simulated photovoltaic parameters (a) V_{oc}, (b) J_{sc}, (c) FF, and (d) PCE as functions of $FASnI_3$ absorber thickness from 500 nm to 1000 nm.*

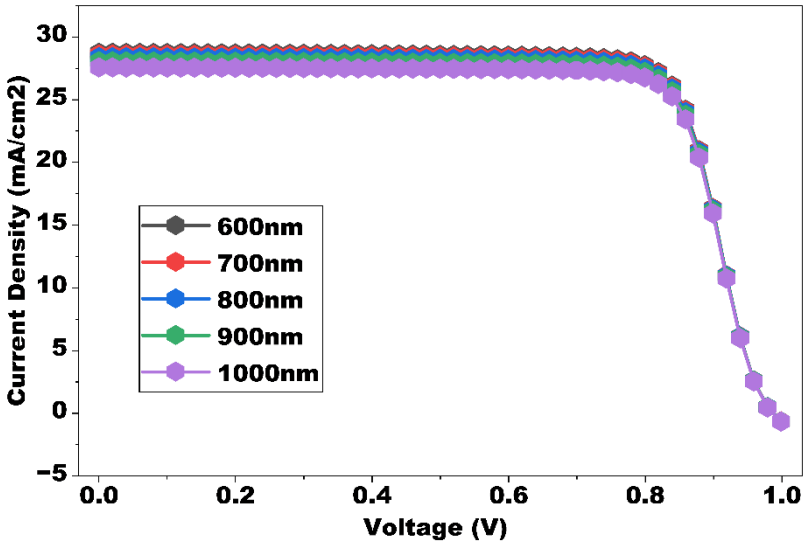


Figure 7: Simulated J–V characteristics for absorber thicknesses from 600 nm to 1000 nm.

The recombination current density as a function of voltage (Fig. 8) is low for all the thicknesses at low forward bias, increasing rapidly at high forward bias, corresponding to the SRH recombination dominance under high injection conditions, where R_{SRH} is maximum at high forward bias, $R_{SRH} = (np - ni^2)/[\tau_p(n + n_1) + \tau_n(p + p_1)]$ [36]. The onset voltage of the recombination surge does not change systematically with thickness, indicating that the recombination mechanism is determined by the trap energy and density, not by the distance that the carrier is transported through the absorber.

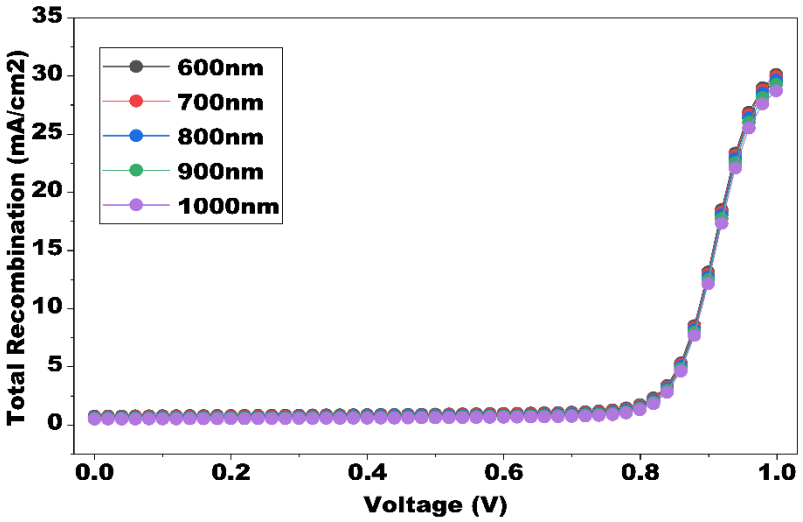


Figure 8: Simulated total recombination current density as a function of applied voltage for absorber thicknesses from 500 nm to 1000 nm.

3.4 Effect of Bulk Defect Density in the $FASnI_3$ Absorber

One of the most important parameters of perovskite solar cells, which directly affects the perovskite absorber's electrical activity, is bulk defect density (N_t). In $FASnI_3$, these defects are mainly associated with tin vacancies, interstitial defects, grain boundaries and the presence of residual Sn^{4+} species resulting from the oxidation of Sn^{2+}, which are known as Shockley–Read–Hall (SRH) recombination centres [10]. With higher trap density, the minority-charge-carrier lifetime reduces, the carrier diffusion length decreases, and non-radiative recombination decreases charge collection and photovoltaic performance. The carrier lifetime is inversely proportional to the trap density ($\tau \propto 1/N_t$); thus, for every order of magnitude increase in N_t, the carrier lifetime decreases by about 1 order of magnitude, and the diffusion length decreases by a factor of $\sqrt{10}$. Therefore, the diffusion length is expected to decrease by over two orders of magnitude when N_t increases from 10^{15} to 10^{20} cm^{-3}, limiting the transport of carriers through the absorber to 1000 nm and significantly reducing the collection efficiency of carriers. This effect was quantified by varying the bulk defect density of the $FASnI_3$ absorber from 1×10^{15} to 1×10^{20} cm^{-3}, while keeping all other simulation parameters fixed: absorber thickness (1000 nm) and other absorber parameters were taken as their default values. The photovoltaic parameters obtained are summarised in Table 4, and the trends of photovoltaic performance are shown in Fig. 9.

Table 4. *Simulated photovoltaic parameters as a function of $FASnI_3$ bulk defect density N_t at 300K.*

N_t (cm^{-3})	V_{oc} (V)	J_{sc} (mA/cm^2)	FF (%)	PCE (%)
1×10^{15}	0.9862	28.73	78.68	22.29
1×10^{16}	0.9857	28.51	76.02	21.37

1×10^{17}	0.9747	26.13	72.47	18.46
1×10^{18}	0.9735	25.62	69.86	17.42
1×10^{19}	0.9582	21.83	60.73	12.70
1×10^{20}	0.9366	16.88	48.80	7.72

The simulated PV parameters with respect to the bulk defect density are shown in Table 4 and Fig. 9. All photovoltaic parameters degrade with the increase of defect density from 1×10^{15} to 1×10^{20} cm^{-3}, which is a progressive increase in the effect of bulk Shockley–Read–Hall (SRH) recombination on carrier transport and collection. With increasing defect density, the carrier lifetime will reduce in direct proportion, which will cause the carrier diffusion length to reduce. As a result, the short-circuit current density of the solar cells decreases continuously from 28.73 to 16.88 mA cm^{-2}, which is a loss of about 41.2%. The sharp drop is in the range 10^{17} to 10^{18} cm^{-3}, meaning that the collection of carriers is increasingly restricted when recombination is the predominant mechanism over diffusion over a large portion of the absorber. The open-circuit voltage decreases from 0.9862 to 0.9366 V (49.6 mV), a relatively small drop. This behaviour suggests that the increase in defect density is the main factor that affects device performance by increasing non-radiative recombination and decreasing the collection of carriers rather than by significantly reducing the built-in potential. The fill factor, on the other hand, drops significantly from 78.68% to 48.80%, which is the highest relative reduction of the PV parameters. The continuing decrease in fill factor is consistent with increasing recombination losses closer to the maximum power point, resulting in a more rounded J-V curve and lower electrical power that can be extracted. This combination of J_{sc}, V_{oc}, and fill factor decreases the power conversion efficiency from 22.29% for 1×10^{15} cm^{-3} to just 7.72% for 1×10^{20} cm^{-3}. Of particular interest, there is an obvious defect-density threshold in the simulated results. The device performance is relatively constant to around 1×10^{16} cm^{-3} with efficiencies greater than 20%. However, beyond 1×10^{17} cm^{-3}, all photovoltaic parameters start to decrease significantly as SRH recombination becomes dominant in the carrier transport. The results in this work indicate that a bulk defect density of ~ 1×10^{16} cm-3 is the practical limit for maintaining high-efficiency $FASnI_3$ solar cells with the current FTO/CeO_2/$FASnI_3$/NiO/Au architecture.

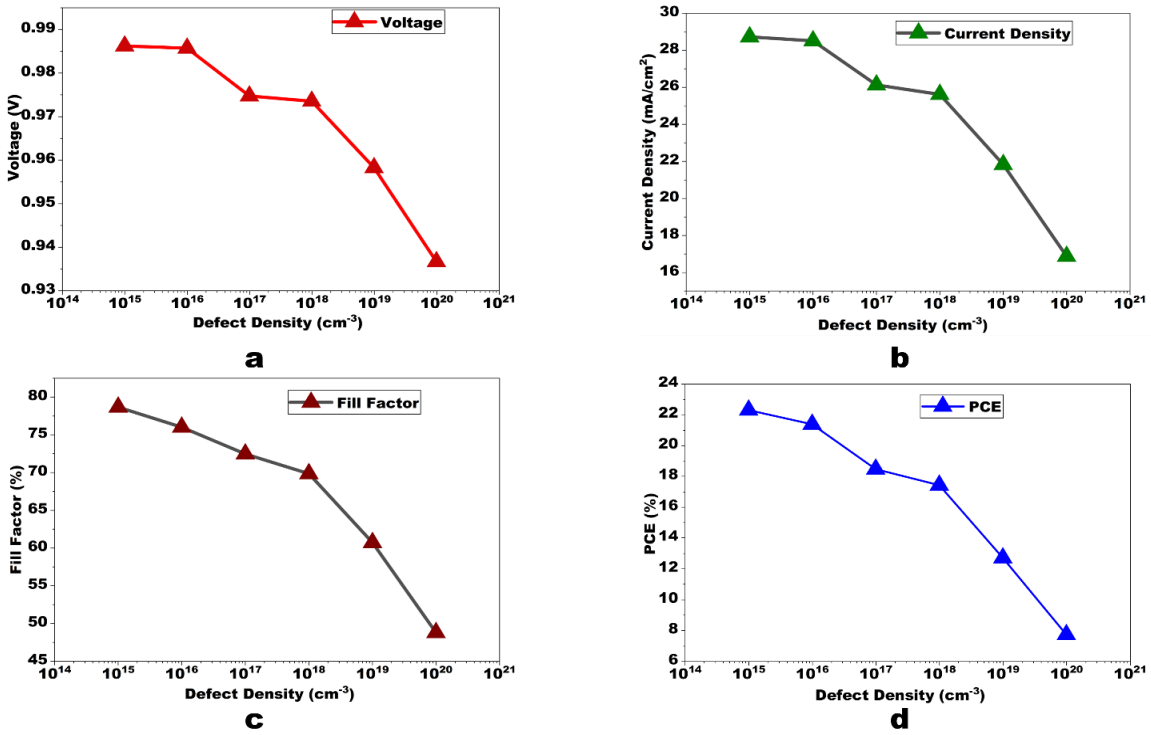


Figure 9: Simulated photovoltaic parameters (a) Voc, (b) Jsc, (c) FF, and (d) PCE as functions of FASnI3 bulk defect density Nt from 10^{15} to 10^{20} cm^{-3}.

3.5 Effect of Operating Temperature (280 K to 310 K)

The device performance is affected by the temperature in a variety of coupled mechanisms in $FASnI_3$: thermal carrier generation, phonon scattering of carriers, ionised-impurity scattering of carriers, SRH trap emission rates, and Varshni bandgap narrowing. The temperature dependence was studied at 280 K, 290 K, 300 K, and 310 K with 1000 nm thickness and a defect density around 10^{15} cm^{-3} Nt. The results are shown in Fig. 10. Voc increases linearly at +0.170 mV/K from 0.9828 V at 280 K to 0.9879 V at 310 K. The simulated positive Voc–temperature coefficient over 280–310 K differs from the commonly reported negative temperature coefficient in many photovoltaic devices. The present calculations establish this trend for the selected SCAPS-1D parameter set, but they do not independently identify the microscopic mechanism responsible for it. In particular, changes in carrier mobility, ionised-impurity scattering and interfacial extraction should not be assigned as causes unless their temperature dependence is explicitly included and tested in the simulation. The Varshni bandgap narrowing slightly increases Jsc (+0.53%). Ionised impurity scattering is the dominant transport mechanism in NiO at temperatures below 300K, which leads to a non-monotonic maximum of 78.68% at 300K. The mobility is also reduced above 300K due to phonon scattering, and the thermally assisted SRH recombination due to the $FASnI_3$/NiO cliff also contributes to the increase in ideality factor, which is a reduction in FF [42]. The corresponding simulated J–V characteristics at 280 K, 290 K, 300 K, and 310 K are shown in Fig. 11.

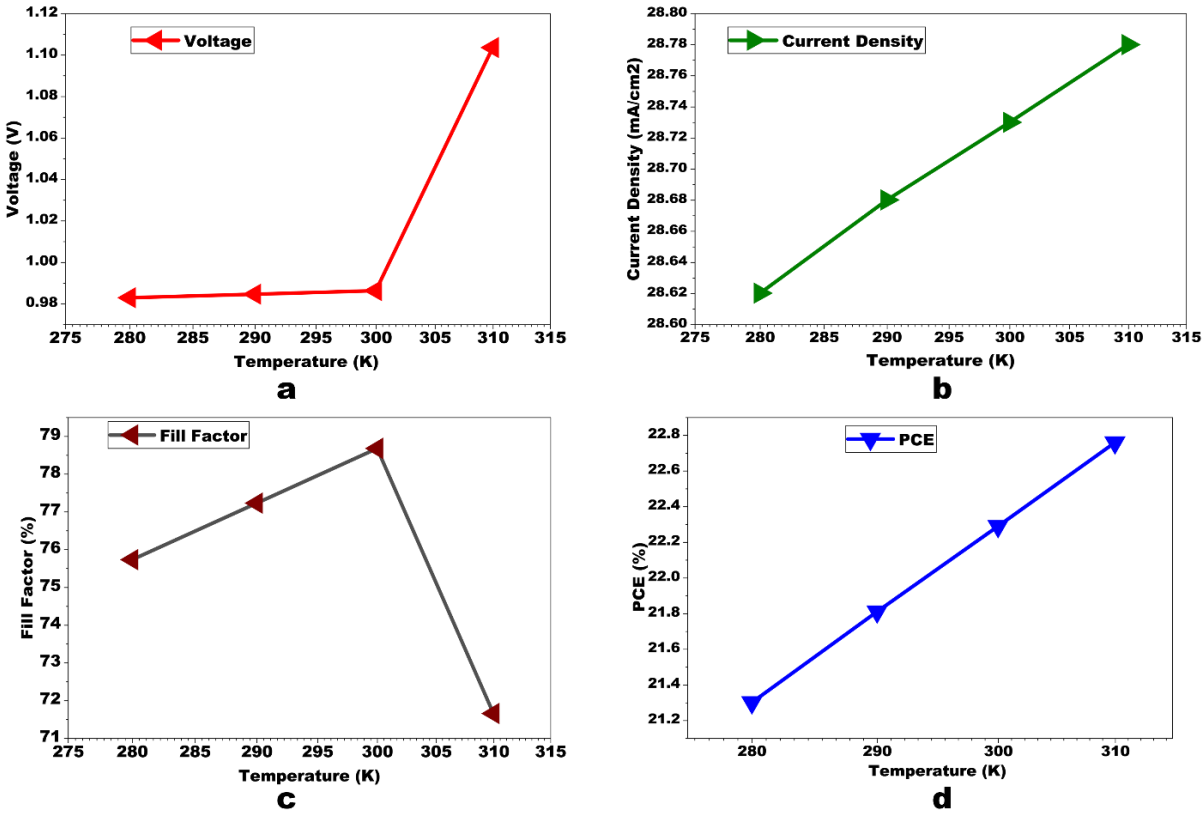


Figure 10: Simulated temperature dependence of (a) Voc, (b) Jsc, (c) FF, and (d) PCE from 280 K to 310 K.

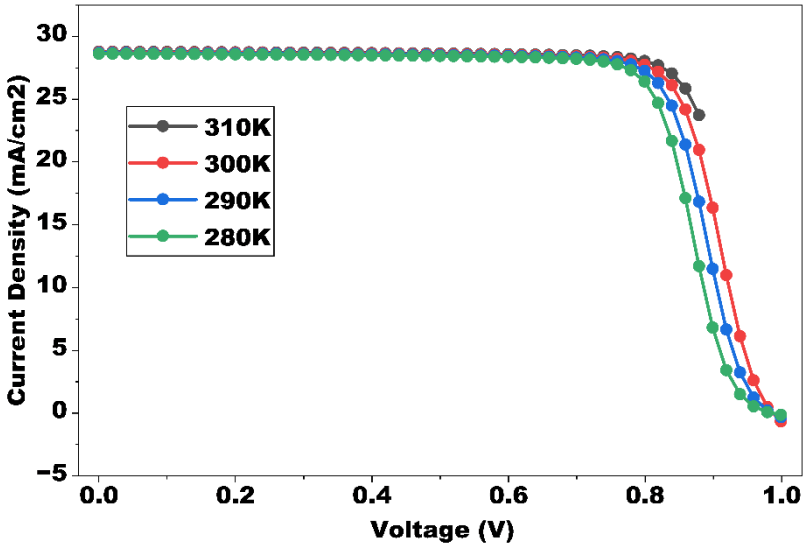


Figure 11: Simulated J–V characteristics at 280 K, 290 K, 300 K, and 310 K.

The recombination current density versus voltage (Fig. 12) shows that the recombination onset shifts to higher/lower voltages with an increase in temperature between 280 and 310 K, consistent with thermally accelerated SRH emission from the trap states [36].

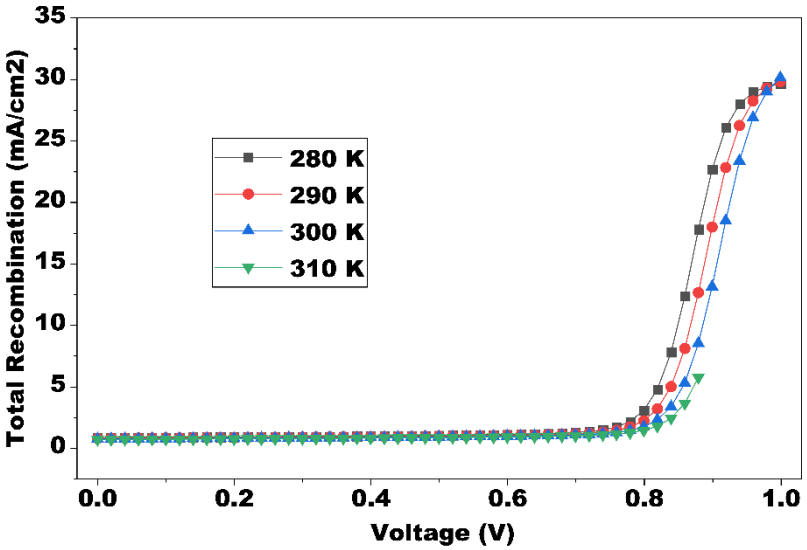


Figure 12: Simulated total recombination current density versus applied voltage at 280 K, 290 K, 300 K, and 310 K.

3.6 Effect of Series Resistance

The effect of series resistance on device performance is simulated and shown in Fig. 13. The fill factor decreases significantly from 78.68% to 53.46% as the series resistance increases from 0 to 10 Ω·cm², indicating that the resistive losses dominate the operation of the device around the maximum power point, consistent with the effect of non-ideal parasitic resistances reported for planar perovskite solar cells simulated in SCAPS-1D [41,42]. This behaviour agrees well with the analytical relationship between fill factor and series resistance. At (Rs = 2) Ω·cm², for instance, the analytical model predicts a reduction of the fill factor of around 5.8 percentage points, and the simulated reduction is 5.22 percentage points. The power conversion efficiency decreases from 22.29% to 15.12% as a result of the reduction in the fill factor. The short-circuit current density is, on the other hand, hardly affected since, under short-circuit conditions, the voltage drop across the series resistance (JRs) is small, and thus the collection of carriers is still efficient even with the higher resistive losses.

The open-circuit voltage is also essentially constant over the range of resistances investigated. With open circuit, the output current is zero, which means the voltage drop across the series resistance (Rs) is also zero, and Voc is independent of Rs. The slight numerical change in Voc from 0.9862 to 0.9867 V is within the numerical precision of the SCAPS calculations and does not imply a physically meaningful change. It is evident that series resistance is an important factor limiting the fill factor and, consequently, the power conversion efficiency, while Voc and Jsc remain comparatively insensitive over the simulated range. The optimisation of the FTO/CeO_2/$FASnI_3$/NiO/Au device architecture is set by maintaining Rs < 2 Ω·cm². The results indicate that the devices are sensitive to the parasitic resistive loss and that for each additional Ω·cm² of series resistance, the device efficiency decreases by about 0.74 percentage points in the range under investigation.

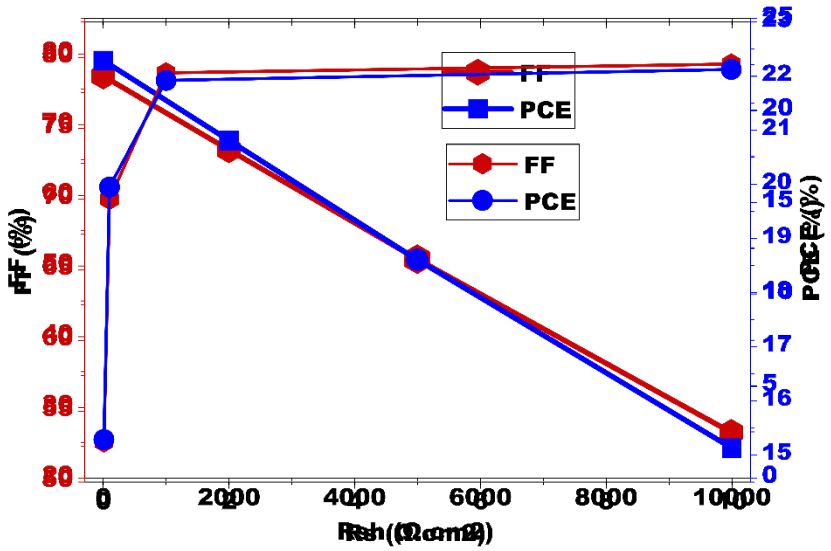


Figure 13: Sensitivity of FF and PCE to series resistance Rs with Rsh = 10,000 Ω·cm².

3.7 Effect of Shunt Resistance

The simulated effect of shunt resistance on the device performance is shown in Fig. 14. The photovoltaic parameters show two different operating regimes with the reduction of shunt resistance from 10,000 to 10 Ω·cm². The device performance is almost unaffected at high shunt resistance values (Rsh $\geqslant$ 1000 Ω • cm²) due to the low leakage current compared to the photogenerated current. However, when the shunt resistance is less than this, leakage current through the shunt pathway rises rapidly, and the performance of the device deteriorates significantly. The Jsc is found to be constant at 28.73 mA/cm² in the range of resistance investigated. This behaviour is directly related to the diode model, as under short-circuit conditions (V = 0) the shunt current becomes essentially zero, thus ensuring that there are no significant losses of current through the parallel leakage path. The open circuit voltage, on the other hand, drops sharply with decreasing shunt resistance, from 0.9847 V at 10,000 Ω·cm² to 0.2866 V at 10 Ω·cm². In extreme shunting conditions, the leakage current may be similar to the current generated by the photons, and the normal open-circuit voltage will not be reached. The analytical approximation Voc = JphRsh gives a voltage of 0.287 V at Rsh=10 (Ω • cm²) which is in excellent agreement with the simulated value of 0.2866 V, thus verifying that the device is in the shunt-dominated regime. The shunt resistance reduction also results in a significant decrease in the fill factor and power conversion efficiency, due to the leakage current diverting the photogenerated carriers from the external circuit. For shunt resistances greater than about 1000 Ω·cm2, the performance of both FF and PCE is fairly constant; below this value, both FF and PCE drop quickly, suggesting a transition from normal photovoltaic operation to leakage-dominated operation. In summary, the results show that a high shunt resistance will be crucial for retaining efficient operation of the device. A practical design target of Rsh $\geqslant$ 1000 Ω • cm² gives a large operating margin over the theoretical critical value of Rsh = 34 Ω • cm² , which assures that leakage currents are kept small enough to be negligible for efficient operation.

Figure 14: Sensitivity of FF and PCE to shunt resistance Rsh with Rs = 0.

3.8. Quantum Efficiency Evaluation

The external quantum efficiency (EQE) spectrum is the probability that a photon at a given wavelength, λ, may generate one electron in the external circuit. It is related to Jsc through the equation, Jsc = q ∫ QE(λ) × Φ(λ) dλ, where Φ(λ) is AM 1.5G photon flux density. The QE spectrum of the baseline device is shown in Fig. 15. The long-wavelength absorption edge is at ~855 nm, which corresponds to the bandgap of $FASnI_3$ (1.45 eV) with λedge = 1240/Eg. The absorption edge of $FASnI_3$ extends 80 nm beyond that of $MAPbI_3$ (= 775 nm, Eg = 1.6 eV), which gives an additional photocurrent of 3 to 4 mA/cm² when compared with the lead halide absorbers [32]. The QE decrease below about 355 nm is due to parasitic absorption of the CeO_2 ETL (bandgap 3.5 eV, absorption onset = 355 nm) and reflection at the FTO/air interface. The QE in the mid-visible range (below unity) is due to reflection and parasitic

absorption in the FTO/CeO_2 layers and recombination near the interfaces; the estimated diffusion length of approximately 2.4 µm (Section 3.1) exceeds the absorber thickness of 1000 nm. The integrated Jsc of the QE spectrum agrees with the directly simulated value of 28.73 mA/cm², which shows the internal consistency of the optical model of SCAPS-1D.

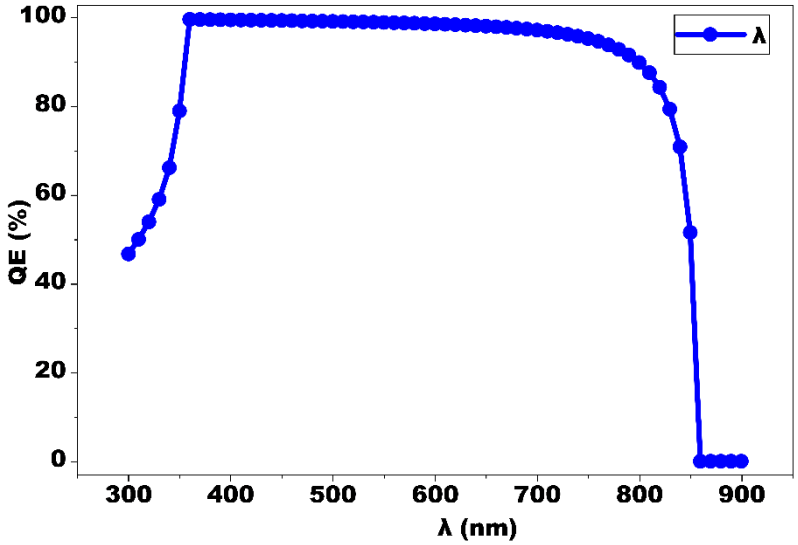


Figure 15: The graph of quantum efficiency against wavelength

3.9 Comparison with Published Literature

The FTO/CeO_2/$FASnI_3$/NiO/Au device achieved a simulated power conversion efficiency of 22.29% under the parameter set used in this study. The comparison in Table 5 places this result alongside previously reported $FASnI_3$-based device simulations; however, differences in material parameters, interface-defect assumptions, contact work functions and optimisation procedures mean that the listed efficiencies should not be interpreted as a direct ranking of device architectures. The lower simulated PCE relative to the FTO/CeO_2/$FASnI_3$/CuI/Au structure reported in reference [15] may be associated with differences in the transport-layer configuration and the band offsets calculated for the present structure. The present study evaluates absorber bandgap, absorber thickness, bulk defect density, temperature and parasitic resistance, together with band alignment and quantum-efficiency spectra. It does not independently quantify the contribution of interface defects to the performance difference. The proposed FTO/CeO_2/$FASnI_3$/NiO/Au architecture has not yet been validated experimentally. The simulation parameters were adopted from published experimental and computational studies, as indicated in Table 1.

Table 5. *Comparison of the simulated photovoltaic parameters of the proposed FTO/CeO_2/$FASnI_3$/NiO/Au device with previously reported lead-free $FASnI_3$ perovskite solar cell architectures.*

Device structure	V_{oc} (V)	J_{sc} (mA/cm²)	FF (%)	PCE (%)	Ref.
FTO/TiO_2/$FASnI_3$/Spiro-OMeTAD/Au	1.81	31.20	33.72	19.08	[16]
ITO/C60/$FASnI_3$/PEDOT: PSS	0.806	25.20	83.62	17.33	[17]

FTO/ZnO/$FASnI_3$/Spiro-OMeTAD/Au	1.06	16.71	85.85	19.80	[15]
FTO/$ZnO_{0.25}S_{0.75}$/$FASnI_3$/Mg $CuCrO_2$/Au	0.773	25.56	76.50	15.11	[18]
FTO/CeO_2/$FASnI_3$/CuI/Au	0.9308	30.68	87.10	24.87	[15]
Au/NiO/$FASnI_3$/$ZnO_{0.25}S_{0.75}$/FTO	0.891	26.82	76.54	18.36	[19]
FTO/CeO_2/$FASnI_3$/NiO/Au	0.9862	28.73	78.68	22.29	This work

4. Conclusions

This work explored the performance of lead-free perovskite solar cell (PSC) in the SCAPS-1D simulator. The energy-band alignment, current–voltage characteristics, recombination current density and quantum-efficiency spectra were used to systematically analyse the effects of absorber bandgap, absorber thickness, bulk defect density, operating temperature, series resistance, and shunt resistance to gain insight into the physical mechanisms that govern device performance. The equilibrium band analysis showed a conduction band cliff of −0.6 eV at the CeO_2/$FASnI_3$ interface and a valence band cliff of −0.19 eV at the $FASnI_3$/NiO interface. The calculated offsets indicate possible interfacial barriers or recombination pathways; however, the interface-defect contribution was not independently varied or quantified in this study. The baseline configuration had a power conversion efficiency of 22.29%, Voc of 0.9862 V, Jsc of 28.73 mA cm^{-2}, and fill factor of 78.68%. The bulk defect density was determined to be the most critical performance-limiting parameter of all those investigated. The power conversion efficiency decreased from 22.29% to 7.72% by increasing the defect density from 10^{15} to 10^{20} cm^{-3}, which increased Shockley–Read–Hall recombination and reduced the estimated carrier diffusion length and carrier-collection efficiency. Results show that the absorber defect density should be kept below ~1 × 10^{16} cm^{-3} to obtain efficiencies greater than 20%, which sets an important quantitative target for fabrication of lead-free $FASnI_3$ device. The absorber bandgap analysis revealed that 1.45 eV is the ideal bandgap for the proposed architecture, and that the thicker the absorber, the more photocurrent was collected; also, the photocurrent increased with absorber thickness over the investigated range, with a progressively smaller gain as optical absorption approached saturation. Across the simulated temperature range, the calculated photovoltaic parameters changed only modestly; this trend is specific to the adopted SCAPS-1D parameter set and should not be interpreted as experimental thermal stability; the parasitic resistance analysis identified practical design limits of < 2 Ω·cm^2 for series resistance and 1000 Ω·cm^2 for shunt resistance to reduce the resistive power loss. The simulated quantum-efficiency spectrum showed an absorption edge at 855 nm, which was consistent with the optical properties of the SCAPS model and the chosen $FASnI_3$ bandgap.

Funding Declaration

This research did not receive any specific grant from funding agencies in the public, commercial, or not-for-profit sectors.

Declarations

Ethics, Consent to Participate, and Consent to Publish declarations: Not applicable.

Competing Interests

The authors declare that they have no competing interests.

Data Availability Statement: The datasets used and/or analysed during the current study are available from the corresponding author on reasonable request.

References

[1] Vakulchuk, R., Overland, I., & Scholten, D. (2020). Renewable energy and geopolitics: A review. Renewable and Sustainable Energy Reviews, 122, Article 109547.

[2] Jena, A., Kulkarni, A., & Miyasaka, T. (2019). Halide perovskite photovoltaics: Background, status, and future prospects. Chemical Reviews, 119. https://doi.org/10.1021/acs.chemrev.8b00539
[3] Shah, N., Shah, A., Leung, P., Khan, S., Sun, K., Zhu, X., & Liao, Q. (2023). A review of third generation solar cells. Processes, 11, Article 1852. https://doi.org/10.3390/pr11061852
[4] Roy, Sinha, N., Tiwari, S., & Khare, A. (2020). A review on perovskite solar cells: Evolution of architecture, fabrication techniques, commercialization issues and status. Solar Energy, 198, 665–688. https://doi.org/10.1016/j.solener.2020.01.080
[5] Nordin, N. A., Mohamed Ansari, M. N., Nomanbhay, S. M., Hamid, N. A., Tan, N. M. L., Yahya, Z., & Abdullah, I. (2021). Integrating photovoltaic (PV) solar cells and supercapacitors for sustainable energy devices: A review. Energies, 14(21), Article 7211. https://doi.org/10.3390/en14217211
[6] Shah, S., Sayyad, M., Khan, K., Guo, K., Shen, F., Sun, J., Tareen, A. K., Gong, Y., & Guo, Z. (2020). Progress towards high-efficiency and stable tin-based perovskite solar cells. Energies, 13, Article 5092. https://doi.org/10.3390/en13195092
[7] Azhakanantham, D., Selvamani, M., Kim, T., & Kesavan, A. (2022). Exploring novel HTL suitable for eco-friendly and high performance FASnI3 photovoltaics. Materials Science and Engineering: B, 284, Article 115909. https://doi.org/10.1016/j.mseb.2022.115909
[8] Saha, P., Singh, S., & Bhattacharya, S. (2024). FASnI3-based eco-friendly heterojunction perovskite solar cell with high efficiency. Micro and Nanostructures, 186, Article 207739. https://doi.org/10.1016/j.micrna.2023.207739
[9] Galve-Lahoz, S., Sánchez-Díaz, J., Echeverría-Arrondo, C., Simancas, J., Rodriguez-Pereira, J., Turren-Cruz, S.-H., Martinez-Pastor, J., Mora-Seró, I., & Delgado, J. (2024). Addressing ambient stability challenges in pure FASnI3 perovskite solar cells through organic additive engineering. Journal of Materials Chemistry A, 12, 21933–21943. https://doi.org/10.1039/D4TA03291H
[10] Karim, M. A., Matsuishi, K., Kayesh, M. E., He, Y., & Islam, A. (2023). Inhibition of Sn2+ oxidation in FASnI3 perovskite precursor solution and enhanced stability of perovskite solar cells by reductive additive. ACS Applied Materials & Interfaces, 15. https://doi.org/10.1021/acsami.3c07903
[11] Mehrabian, M., Taleb-Abbasi, M., & Akhavan, O. (2024). Using Cu2O/ZnO as two-dimensional hole/electron transport nanolayers in unleaded FASnI3 perovskite solar cells. Materials, 17, Article 1064. https://doi.org/10.3390/ma17051064
[12] Dong, J., Feng, X., Jia, J., Shi, B., Wu, Y., & Cao, B. (2023). Annealing free CeO2 electron transport layer for efficient perovskite solar cells. Journal of Solid State Chemistry, 317(Part A), Article 123661. https://doi.org/10.1016/j.jssc.2022.123661
[13] Deepika, Singh, A., Verma, U. K., & Ameen, S. (2024). Optimization of lead-free materials-based perovskite solar cell using SCAPS-1D simulation. Journal of Physics and Chemistry of Solids, 186, Article 111817. https://doi.org/10.1016/j.jpcs.2023.111817
[14] Ashfaq, A., Tahir, S., Mushtaq, S., Alqurashi, R. S., Haneef, M., Almousa, N., Rehman, U. U., & Bonilla, R. S. (2023). Comparative performance analysis of Cs2TiX6 (X = Br-, Cl-, I-) lead-free perovskite solar cells incorporating single, double and triple layer halides by SCAPS-1D. Materials Today Communications, 35, Article 106016. https://doi.org/10.1016/j.mtcomm.2023.106016
[15] Ahmad, M., Ibrahim Takai, Z., & Zangina, T. (2026). Sensitivity-Based Performance Optimisation of a Lead-Free Formamidinium Tin Iodide (Fasni3) Perovskite Solar Cell Using Scaps-1d Simulation . FUDMA Journal of Sciences, 10(19), 269-279. https://doi.org/10.33003/fjs-2026-1019-5914
[16] Singh, N. K., Agarwal, A., Singh, A. K., & Singh, S. N. (2024). Design and performance evaluation of eco-friendly FASnI3/CsSn0.5Ge0.5I3 based perovskite solar cell with distinct charge transport layer: A computational modeling. Solar Energy, 268, Article 112256. https://doi.org/10.1016/j.solener.2023.112256
[17] Shukla, R., Ranjan, R., & Pandey, S. (2021). Theoretical study of charge carrier lifetime and recombination on the performance of eco-friendly perovskite solar cell. IEEE Transactions on Electron Devices, 68, 3446–3452. https://doi.org/10.1109/TED.2021.3078063
[18] El Arfaoui, Y., Khenfouch, M., & Habiballah, N. (2024). Optimization of all Pb-free perovskite CsGeI3/FASnI3 tandem solar device with 30.42% efficiency: Numerical simulation using SCAPS. Optik, 300, Article 171638. https://doi.org/10.1016/j.ijleo.2024.171638
[19] Mattaparthi, S., Sinha, D., Bhura, A., & Khosla, R. (2023). Design of an eco-friendly perovskite Au/NiO/FASnI3/ZnO0.25S0.75/FTO device structure for solar cell applications using SCAPS-1D. Results in Optics, 12, Article 100444. https://doi.org/10.1016/j.rio.2023.100444
[20] Nalianya, M. A., Awino, C., Barasa, H., Odari, V., Gaitho, F., Omogo, B., & Mageto, M. (2021). Numerical study of lead free CsSn0.5Ge0.5I3 perovskite solar cell by SCAPS-1D. Optik, 248, Article 168060. https://doi.org/10.1016/j.ijleo.2021.168060
[21] Meskini, M., & Asgharizadeh, S. (2024). Performance simulation of the perovskite solar cells with Ti3C2 MXene in the SnO2 electron transport layer. Scientific Reports, 14(1). https://doi.org/10.1038/s41598-024-56461-z

[22] Huang, L., Sun, X., Li, C., Xu, R., Xu, J., Du, Y., Wu, Y., Ni, J., Cai, H., Li, J., Hu, Z., & Zhang, J. (2016). Electron transport layer-free planar perovskite solar cells: Further performance enhancement perspective from device simulation. Solar Energy Materials and Solar Cells, 157. https://doi.org/10.1016/j.solmat.2016.08.025
[23] Bhuvaneswari, P., & Sriramalakshmi, P. (2025). Lead-free p-n homojunction Cs-doped and pure FASnI3-based perovskite solar cells – A performance analysis using SCAPS 1D simulator. Results in Engineering, 26, Article 104779. https://doi.org/10.1016/j.rineng.2025.104779
[24] Uddin, M., Hossain, M. K., Uddin, M., Toki, G. F., Ouladsmane, M., Rubel, M. H. K., Tishkevich, D., Sasikumar, P., Haldhar, R., & Pandey, R. (2024). An in-depth investigation of the combined optoelectronic and photovoltaic properties of lead-free Cs2AgBiBr6 double perovskite solar cells using DFT and SCAPS-1D frameworks. Advanced Electronic Materials, 10, Article 2300751. https://doi.org/10.1002/aelm.202300751
[25] Minemoto, T., & Murata, M. (2015). Theoretical analysis on effect of band offsets in perovskite solar cells. Solar Energy Materials and Solar Cells, 133, 8–14. https://doi.org/10.1016/j.solmat.2014.10.036
[26] Schulz, P., Edri, E., Kirmayer, S., Hodes, G., Cahen, D., & Kahn, A. (2014). Interface energetics in organo-metal halide perovskite-based photovoltaic cells. Energy & Environmental Science, 7(4), 1377–1381. https://doi.org/10.1039/c4ee00168k
[27] Kiermasch, D., et al. (2016). Improved charge carrier lifetime in planar perovskite solar cells by bromine doping. Scientific Reports, 6, Article 39333. https://doi.org/10.1038/srep39333
[28] Almora, O., Baran, D., Bazan, G. C., Cabrera, C. I., Erten-Ela, S., Forberich, K., Guo, F., Hauch, J., Ho-Baillie, A. W. Y., Jacobsson, T. J., Janssen, R. A. J., Kirchartz, T., Kopidakis, N., Loi, M. A., Lunt, R. R., Mathew, X., McGehee, M. D., Min, J., Mitzi, D. B., Nazeeruddin, M. K., Nelson, J., Nogueira, A. F., Paetzold, U. W., Rand, B. P., Rau, U., Snaith, H. J., Unger, E., Vaillant-Roca, L., Yang, C., Yip, H.-L., & Brabec, C. J. (2023). Device performance of emerging photovoltaic materials (Version 3). Advanced Energy Materials, 13, Article 2203313. https://doi.org/10.1002/aenm.202203313
[29] Warby, J., Shah, S., Thiesbrummel, J., Gutierrez-Partida, E., Lai, H., Alebachew, B., Grischek, M., Yang, F., Lang, F., Albrecht, S., Fu, F., Neher, D., & Stolterfoht, M. (2023). Mismatch of quasi-Fermi level splitting and Voc in perovskite solar cells. Advanced Energy Materials, 13, Article 2303135. https://doi.org/10.1002/aenm.202303135
[30] Bhavsar, K., & Lapsiwala, P. (2021). Numerical simulation of perovskite solar cell with different material as electron transport layer using SCAPS-1D software. Semiconductor Physics, Quantum Electronics and Optoelectronics, 24, 341–347. https://doi.org/10.15407/spqeo24.03.341
[31] Stranks, S. D., et al. (2013). Electron-hole diffusion lengths exceeding 1 micrometer in an organometal trihalide perovskite absorber. Science, 342, 341–344. https://doi.org/10.1126/science.1243982
[32] Noman, M., Shahzaib, M., Jan, S. T., Khan, Z., Ismail, M., & Khan, A. D. (2024). Optimizing band gap, electron affinity, and carrier mobility for improved performance of formamidinium lead tri-iodide perovskite solar cells. Materials Science and Engineering: B, 300, Article 117114. https://doi.org/10.1016/j.mseb.2023.117114
[33] Kanwal, S., Illahi, A., Anis-ur-Rehman, M., Kaleem, M., Ahmed, W., Javed, Z., & Nasir, A. (2025). Unveiling the photovoltaic potential of lead-free Bi2Ca2CoO6 perovskite oxide solar cells. Journal of Science: Advanced Materials and Devices, Article 101093. https://doi.org/10.1016/j.jsamd.2025.101093
[34] Carrera-Crespo, J., Fuentes-Camargo, I., Palma, R., García Pérez, U. M., Vazquez-Arenas, J., Chairez, I., & Poznyak, T. (2021). Unrevealing the effect of transparent fluorine-doped tin oxide (FTO) substrate and irradiance configuration to unmask the activity of FTO-BiVO4 heterojunction. Materials Science in Semiconductor Processing, 128, Article 105717. https://doi.org/10.1016/j.mssp.2021.105717
[35] Katubi, K., Ng, S. S., Pakhuruddin, M. Z., Alkhalayfeh, M., Abubaker, S., & Al-Soeidat, M. (2023). Over 35% efficiency of three absorber layers of perovskite solar cells using SCAPS 1-D. Optik, 297, Article 171579. https://doi.org/10.1016/j.ijleo.2023.171579
[36] Jokar, E., Chien, C.-H., Fathi, A., Rameez, M., Chang, Y.-H., & Diau, E. W.-G. (2018). Slow surface passivation and crystal relaxation with additives to improve device performance and durability for tin-based perovskite solar cells. Energy & Environmental Science, 11(9), 2353–2362. https://doi.org/10.1039/c8ee00956b
[37] Neukom, M. T., et al. (2019). Consistent device simulation model describing perovskite solar cells in steady-state, transient, and frequency domain. ACS Applied Materials & Interfaces, 11, 23320–23328. https://doi.org/10.1021/acsami.9b04991
[38] Green, M. A. (1981). Solar cell fill factors: General graph and empirical expressions. Solid-State Electronics, 24(8), 788–789. https://doi.org/10.1016/0038-1101(81)90062-9

[39] Kirchartz, T., & Rau, U. (2018). What makes a good solar cell? Advanced Energy Materials, 8, Article 1703385. https://doi.org/10.1002/aenm.201703385
[40] Abdelaziz, S., Zekry, A., Shaker, A., & Abouelatta, M. (2020). Investigating the performance of formamidinium tin-based perovskite solar cell by SCAPS device simulation. Optical Materials, 101, Article 109738. https://doi.org/10.1016/j.optmat.2020.109738
[41] Hosseini, S. R., Bahramgour, M., Yardani Sefidi, P., Tabatabaei Mashayekh, A., Moradi, A., Delibas, N., Hosseini, M. G., & Niaei, A. (2022). Investigating the effect of non-ideal conditions on the performance of a planar CH3NH3PbI3-based perovskite solar cell through SCAPS-1D simulation. Heliyon, 8(11), Article e11471. https://doi.org/10.1016/j.heliyon.2022.e11471
[42] Burgelman, M., Nollet, P., & Degrave, S. (2000). Modelling polycrystalline semiconductor solar cells. Thin Solid Films, 361–362, 527–532. https://doi.org/10.1016/S0040-6090(99)00825-1